Multicolor structured illumination microscopy and quantitative control of coherent light with a digital mirror device

Peter T. Brown[1], **Rory Kruithoff**[1], **Gregory J. Seedorf**[2], **and Douglas P. Shepherd**[1,✉]

[1]Department of Physics and Center for Biological Physics, Arizona State University, Tempe, AZ 85287, USA
[2]Department of Pediatrics and Pediatric Heart Lung Center, University of Colorado Anschutz Medical Campus, Aurora, CO 80045, USA

Abstract

We demonstrate structured illumination microscopy (SIM) at three wavelengths using a digital mirror device (DMD), an approach which has not previously been realized due to the DMD's blazed grating effect. Previous approaches to SIM using a DMD have used one color of coherent light or multiple colors via incoherent projection. To address this challenge, we develop a forward model of DMD diffraction, a forward model of coherent pattern projection, and identify an experimentally feasible configuration for three common fluorophore wavelengths. Based on these results, we constructed a custom DMD SIM and created an open-source software suite to simulate, calibrate, execute, and reconstruct 2D linear SIM data. We validate this approach by demonstrating resolution enhancement for known calibration samples and fixed cells.

Correspondence: ***douglas.shepherd @asu.edu***

1: Introduction

The development of super-resolution (SR) microscopy has enabled optical study of biological systems below the diffraction limit, on the $10\,\mathrm{nm}$–$200\,\mathrm{nm}$ scale. Despite the promise of sub-diffraction limited information to advance understanding of the molecular interactions that govern biological regulation, many super-resolution techniques are only applicable under a limited set of circumstances. All SR methods impose a trade-off between imaging speed, resolution, sample preparation, and fluorophore photophysics requirements. For example, single molecule localization microscopy (SMLM) trades temporal resolution for spatial resolution, requiring fixed samples and repeated imaging of fluorophores with specific photophysics (1, 2). Computational methods that infer SR information from fluctuating signals relax the above requirements, but require acquisition, processing, and merging of many imaging frames (3, 4). Recently coined 'modulation enhanced' localization microscopy (meLM) relies on precise pattern formation to control reversible saturation or repeated excitation of fluorophores (5). While structured illumination microscopy (SIM) relies on the same precise pattern formation as meLM methods, SIM itself imposes no specific sample requirements. This makes SIM a versatile technique for general purpose SR measurements. The trade-off for this flexibility is a modest increase in high frequency content, with the ideal resolution reaching twice the diffraction limit in linear SIM.

SIM operates by using a sinusoidal illumination pattern to down mix spatial frequency information beyond the diffraction limit below the microscope's cut-off frequency, taking advantage of the Moiré effect. It was first proposed as an SR technique in (6, 7), but a similar technique had been previously exploited for optical sectioning (OS) (8–10). Initial implementations achieved SR in the lateral direction only (2D-SIM) (11, 12), while later approaches also enhanced the axial resolution (3D-SIM) (13–15). Early experiments utilized diffraction gratings to produce SIM patterns and required both separate paths for multiple colors and physical translation and rotation, which severely limited their speed (15). Various advances in LCD and ferroelectric spatial light modulators (SLM's), sCMOS cameras, and GPU's have enabled much faster 2D (16–21) and 3D SIM (22), and multicolor SIM with a single optical path (23).

Digital mirror devices (DMD's) are a promising alternative to SLM's for coherent SIM which offer several advantages, including a potential factor of 5–10 imaging rate increase, less experimental complexity, and lower cost (24–26). However, DMD use is currently limited by a computationally

expensive forward model (25) to evaluate the blazed grating effect, which imposes severe restrictions on multicolor operation. To date, all published work has used incoherent projection (27, 28) or one coherent wavelength (25, 26, 29).

Here, we overcome these difficulties to realize three wavelength, 2D linear SIM using coherent light and a DMD. We achieve this by creating analytical forward models of light diffraction off of a DMD and pattern projection to the sample plane. We use these models to design an optical configuration that satisfies the unique requirements that a DMD imposes when used as a diffractive optic for multiple wavelengths. This framework allows us to create a calibration routine to directly map the optical transfer function (OTF) of the system without the need to estimate it from sub-diffraction limited fluorescent microspheres. We provide simulations and experimental verification of this framework for calibration and fixed samples.

The tools we develop here may benefit other experiments that rely on quantitative multicolor pattern projection with DMD's. For example diffraction tomography techniques, some of which employ DMD's (30), rely on projecting plane waves through a sample at varied angles and obtaining a high quality refractive index map depends on precise calibration of the projection device (31). DMD's have been explored for fast single-pixel imaging (32), where quantitative knowledge of the pattern formation could improve reconstruction algorithms and multicolor operations. DMD's are also used to generate arbitrary optical potentials in quantum simulation with ultracold atoms (33, 34), and extracting quantitative information from these experiments requires precise calibration of the potential.

2: Principles of multicolor DMD SIM using coherent light

DMD's can reach frame rates of up to $20\,\mathrm{kHz}$, exceeding the rate achievable in ferroelectric and liquid crystal SLM's by a factor of $\sim$5 and $\sim$10 respectively. Furthermore, currently available DMD's are a factor of 2–10 less expensive than these other options and unlike ferroelectric SLM's, do not require the pattern to be inverted every $\sim 100\,\mathrm{ms}$. Finally, the amplitude-only modulation characteristic of the DMD allows fast, well-defined diversion of the illumination beam from the sample, making an additional fast shutter unnecessary. Leveraging the advantages of the DMD in a multicolor setting requires a tractable and complete forward model of DMD operation. To this end, we derive an analytical forward model of DMD diffraction and pattern projection. This provides an alternative framework to a previously published numerical simulation approach (25). We use our approach to perform detailed calculations of DMD diffraction of SIM patterns and apply these to directly measure the OTF and realize multicolor coherent SIM.

2.1. Multicolor DMD diffraction model. To develop the DMD forward model, we calculate the diffracted light profile for an incident plane wave in the Fraunhofer approximation by considering the phase shift introduced by each point on the micromirror surfaces (25, 35, 36). We adopt the same coordinate system as (25), where the DMD normal is along the $-\hat{\mathbf{z}}$ direction, the DMD mirrors are organized in a regular grid aligned with the $\hat{\mathbf{x}}$ and $\hat{\mathbf{y}}$ directions, and the micromirrors swivel about an axis along the $\mathbf{x}\,\hat{+}\,\mathbf{y}$ direction. For a plane wave of wave vector $k = 2\pi/\lambda$ incident along direction $\hat{\mathbf{a}}$, the diffracted electric field in direction $\hat{\mathbf{b}}$ is

$$\begin{aligned} E(\hat{\mathbf{b}}) &= E_o \sum_{m_x,m_y} \exp\Big(ikd(m_x,m_y)\cdot(\hat{\mathbf{a}}-\hat{\mathbf{b}})\Big) \\ &\times\ w^2 \operatorname{sinc}\left(\frac{kw}{2}A_+(\gamma_{m_x,m_y})\right)\operatorname{sinc}\left(\frac{kw}{2}A_-(\gamma_{m_x,m_y})\right) \qquad \textbf{(1)} \\ A_\pm(\gamma,\hat{\mathbf{a}}-\hat{\mathbf{b}}) &= \frac{1\pm\cos\gamma}{2}(a_x-b_x)+\frac{1\mp\cos\gamma}{2}(a_y-b_y)\mp\frac{\sin\gamma}{\sqrt{2}}(a_z-b_z), \qquad \textbf{(2)} \end{aligned}$$

where γ_{m_x,m_y} is the angle the mirror at position (m_x,m_y) makes with grating normal, w is the mirror width, and d is the spacing between adjacent mirrors. At each mirror γ takes one of two values: either 12° ("on") or -12° ("off"). Here the sinc envelope expresses the effect of rays interfering from the same micromirror, and the sum represents rays interfering from different micromirrors.

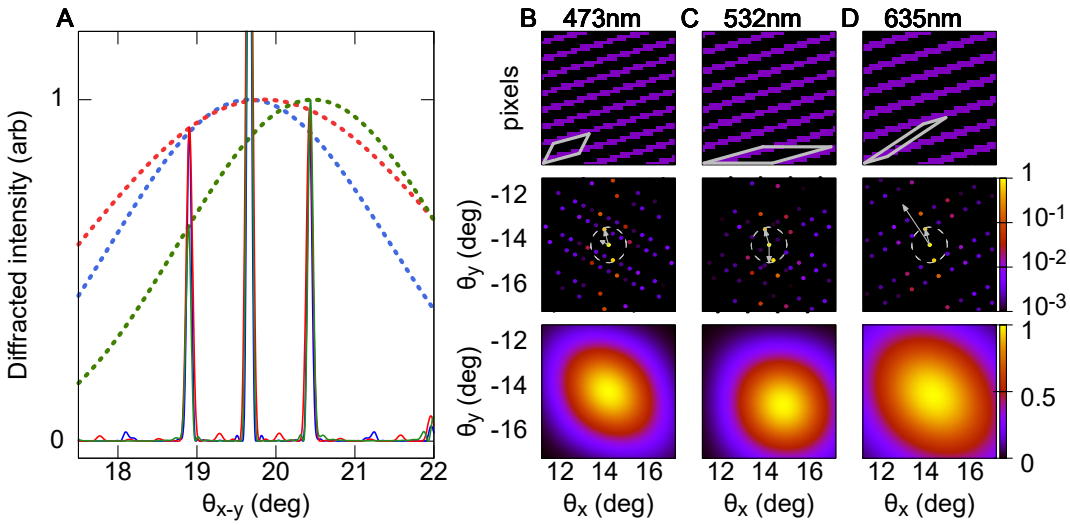

Fig. 1. A. Diffracted intensity for $\theta^a_{x-y} = 43.66°$ and $\lambda = 473\,\mathrm{nm}$ (blue), $\theta^a_{x-y} = -3.53°$ and $532\,\mathrm{nm}$ (green), and $\theta^a_{x-y} = 43.86°$ and $635\,\mathrm{nm}$ (red). For these input angles, $473\,\mathrm{nm}$ satisfies the Blaze condition, and $635\,\mathrm{nm}$ satisfies it to within a fraction of a degree. $532\,\mathrm{nm}$ shows a larger deviation, visible in the shift of the envelope center and the asymmetry in the diffraction peaks. To ensure the diffraction peaks for all colors appear at the same location and along the $\theta_x = -\theta_y$ line the patterns simulated here have periods of 5, 5.62, and 6.71 mirrors which are not commensurate with the pixel lattice. **B**. DMD mirror pattern showing "on" mirrors (purple), "off" mirrors (black), and one unit cell (gray outline) for $\mathbf{r}_1 = (11, 3)$ and $\mathbf{r}_2 = (3, 6)$ (upper panel). Diffracted intensity from the DMD using $473\,\mathrm{nm}$ light incident at $\theta_{x-y} = 43.66°$ shown on a log scale. The maximum acceptance angle (Gray circle) and reciprocal vectors (Gray arrows) are shown (center panel). The envelope function illustrating where the blaze condition is satisfied, shown with a linear scale. **C**. panels the same as B, but for $532\,\mathrm{nm}$ light incident at $-3.53°$ with $\mathbf{r}_1 = (18, 5)$ and $\mathbf{r}_2 = (21, 0)$. **D**. $635\,\mathrm{nm}$ light incident at $43.86°$ with $\mathbf{r}_1 = (7, 2)$ and $\mathbf{r}_2 = (18, 12)$.

wavelength	θ^a_{x-y}	diffraction order	η^2	m
$473\,\mathrm{nm}$	$43.66°$	(4, 4)	1	1
$532\,\mathrm{nm}$	$-3.53°$	(-4, -4)	0.95	0.9997
$635\,\mathrm{nm}$	$43.86°$	(3, 3)	0.66	0.979

Table 1. Comparison of modulation contrast degredation in SIM patterns due to violation of the blaze condition versus wavelength for the 5 mirror period patterns shown in Fig. 1.

We display patterns $P(m_x, m_y)$ on the device, where we take $P = 0$ on "off" mirrors at angle $-\gamma$, or $P = 1$ on "on" mirrors at angle γ. Then we can rewrite the electric field

$$\begin{aligned} E(\hat{\mathbf{b}}) &= \tilde{P}\left(\frac{d}{\lambda}(\hat{\mathbf{a}} - \hat{\mathbf{b}})\right) E_o w^2 \operatorname{sinc}\left(\frac{kw}{2} A_+(\gamma)\right) \operatorname{sinc}\left(\frac{kw}{2} A_-(\gamma)\right) \\ &+ \tilde{P}_c\left(\frac{d}{\lambda}(\hat{\mathbf{a}} - \hat{\mathbf{b}})\right) E_o w^2 \operatorname{sinc}\left(\frac{kw}{2} A_+(-\gamma)\right) \operatorname{sinc}\left(\frac{kw}{2} A_-(-\gamma)\right), \end{aligned} \tag{3}$$

where $\tilde{P}$ is the discrete Fourier transform (DFT) of P, and $P_c = 1 - P$. The complete information about the pattern is contained in a discrete set of output angles (frequencies) given by the DFT frequencies

$$\hat{\mathbf{a}} - \hat{\mathbf{b}} = \frac{\lambda}{d}\left(\frac{n_x}{N_x}, \frac{n_y}{N_y}\right), \; n_x, n_y \in \mathbb{Z}. \tag{4}$$

When n_x (n_y) is a multiple of N_x (N_y) eq. 4 is the diffraction condition for the underlying grating. Other frequencies are generated by the DMD pattern itself. For a finite pixel grid, intermediate frequencies can be calculated from the DFT, using an approach similar to the Whittaker-Shannon interpolation formula.

For incorporating the DMD into the complete response of an optical system, it is convenient to recast eqs. 3 and 4 as defining the (electric field) optical transfer function of the DMD,

$$E(\mathbf{f}) = \tilde{P}(\mathbf{f}) H_{\mathrm{DMD}}(\mathbf{f}) \tag{5}$$

$$H_{\mathrm{DMD}}(\mathbf{f}) = w^2 \operatorname{sinc}\left[A_+\left(\gamma, \hat{\mathbf{a}} - \hat{\mathbf{b}}(\mathbf{f})\right)\right] \operatorname{sinc}\left[A_-\left(\gamma, \hat{\mathbf{a}} - \hat{\mathbf{b}}(\mathbf{f})\right)\right] \tag{6}$$

where $\mathbf{f}$ is the spatial frequency of the DMD image, $\mathbf{b}_o$ is the vector satisfying the diffraction condition, and $\hat{\mathbf{b}}$ is the output unit vector, given by $\hat{b}_{x,y} = (b_o)_{x,y} + \lambda f_{x,y}$. We ignore the "off"-state mirrors in

this equation, as we are only considering frequencies near a single solution of the diffraction condition, and the sinc envelopes for the "on" mirror state and "off" mirror state blaze conditions are typically well separated.

Equation 5 constitutes a complete forward model of DMD diffraction. The expressions obtained here remove the need to numerically evaluate integrals or perform other expensive numerical simulations to determine DMD diffraction. It is only necessary to calculate a discrete Fourier transform, solve for output angles, and evaluate the sinc factor.

Before applying this forward model to the DMD SIM patterns, we consider its consequences for multicolor DMD operation. We first specialize to the plane in which the micromirrors swivel (i.e. the $(x-y)\,z$ plane), which simplifies both the experimental setup and theoretical analysis because light that is incident in this plane will have its primary diffraction orders in the same plane. Let $\theta_x^{a,b}$ and $\theta_y^{a,b}$ be the angles between $\hat{\mathbf{a}}$ or $\hat{\mathbf{b}}$ and the DMD normal when projecting onto the xz and yz planes. The $(x-y)\,z$ plane is defined by $\theta_x^{a,b} = -\theta_y^{a,b}$, and the angle between in-plane rays the DMD normal is $\theta^{a,b} = \arctan[\sqrt{2}\tan(\theta_x^{a,b})]$ (25). For light incoming and outgoing in this plane, the blaze and diffraction conditions reduce to (35),

$$\theta^a - \theta^b = 2\gamma \tag{7}$$

$$\sin\theta^a - \sin\theta^b = \sqrt{2}\frac{\lambda_i}{d}n_i, \tag{8}$$

where i indexes the different wavelengths. The blaze condition (eq. 7) is the angle where the law of reflection is satisfied for light incident on a single micromirror (35). For N wavelengths, this is a system of $N+1$ equations with two angles and N diffraction orders as free parameters. For $N=1$ this system can be solved for small diffraction orders, and the maximum achievable diffraction order can be found by maximizing the left-hand-side of eq. 8, which occurs at $\bar{\theta}^a = \arctan[(\cos 2\gamma - 1)/\sin 2\gamma]$.

To realize multicolor operation we must solve this system for $N > 1$, which we achieve by solving the blaze and diffraction conditions for λ_1, and then attempting to satisfy $\frac{\lambda_i}{\lambda_j} = \frac{n_j}{n_i}$. This ratio condition can be solved by finding rational approximations to each of these, $\lambda_i/\lambda_1 = p_i/q_i$. Then an approximate solution is obtained by taking $n_1 = \mathrm{lcm}(p_1, ..., p_n)$ and $n_i = q_i n_1/p_i$. The small deviation between the rational approximation and the wavelength ratio must be accounted for by changing the input angle of the incident light, which entails slight violations of the blaze condition. This can be achieved by using a galvanometric mirror or projecting different colors from spatially separated sources.

For our DMD parameters, $d = 7.56\,\mu\mathrm{m}$ and $\gamma = 12°$, two color operation can be achieved using $\lambda_1 = 473\,\mathrm{nm}, \lambda_2 = 635\,\mathrm{nm}$, by approximating $\lambda_2/\lambda_1 \sim 4/3$ which implies $n_1 = 4, n_2 = 3$. Adding a third wavelength, $\lambda_3 = 532\,\mathrm{nm}$, using this approach is challenging because the smallest rational approximation with less than $10\,\%$ error is $\lambda_3/\lambda_1 \sim 8/7$, implying $n_1 = 8, n_2 = 7, n_3 = 6$. However, the maximum diffraction orders allowed by eqs. 7 and 8 are $n_{\mathrm{max}} = 4, 3, 3$ respectively.

One final possibility is to inject additional colors using the other DMD mirror state. Supposing we have already chosen values for some number of colors using one state, then we can still check if the other state satisfies the blaze and diffraction conditions for $-\gamma$. We can write the new input angle in terms of the fixed output angle and the input angle of the fixed orders, $\tilde{\theta}^a = \theta^b - 2\gamma = \theta^a - 4\gamma$. We can take advantage of this provided

$$\sin(\theta^a - 4\gamma) - \sin(\theta^a - 2\gamma) = \sqrt{2}\frac{\lambda}{d}n. \tag{9}$$

Taking advantage of both the "on" and "off" state mirrors, we achieve three color operation with a DMD. We satisfy the blaze condition for both $\lambda = 473\,\mathrm{nm}$ and $635\,\mathrm{nm}$ with $\theta^a = \sim 43°$ and $\theta^b = \sim 19°$. This takes advantage of the close overlap between the $(n_x, n_y) = (4,4)$ and $(3,3)$ diffraction orders for the two colors respectively. We inject $532\,\mathrm{nm}$ light using $\theta^a = -3.5°$ and the $(n_x, n_y) = (-4,-4)$ order from the "off" mirrors. For the $532\,\mathrm{nm}$ light, eq. 9 predicts $n \approx -4.15$. Overlapping the $532\,\mathrm{nm}$ diffraction with the other colors requires a deviation of about $1.5°$ from the blaze condition. Perfect alignment of the $n = -4$ order occurs near $550\,\mathrm{nm}$. The effect of deviations from the blaze condition in the three colors is illustrated in Fig. 1.

In our experimental setup (Supplemental Note 1) we use a voice coil mirror in a conjugate plane to the DMD to adjust the incoming beam angle for each color, ensuring optimal overlap of the diffracted orders. For the $473\,\mathrm{nm}$ and $635\,\mathrm{nm}$ beams, this adjustment is a fraction of a degree. For the $532\,\mathrm{nm}$ beam, this is a gross adjustment to direct the beam to a separate optical path.

For each color, we quantify the degradation in SIM modulation contrast entailed by violation of the blaze condition. Let η be the imbalance between the two components of the diffracted electric field that interfere to produce the SIM pattern. The pattern modulation contrast is the ratio of amplitudes of the high frequency and DC components,

$$m = \frac{2\eta}{1+\eta^2}. \tag{10}$$

The pattern contrast depends on the angle of the SIM pattern, ranging from a minimum along the $\theta_x = -\theta_y$ direction to a maximum along the $\theta_x = \theta_y$ direction. We summarize the worst case contrast for our parameters in table 1, where we find high contrast is achievable in spite of the modest violation of the blaze condition at $532\,\mathrm{nm}$.

2.2. DMD SIM forward model. To understand SIM operation we apply our forward model to a set of mirror patterns commonly employed to generate sinusoidal illumination profiles. SIM patterns are designed to be periodic to maximize diffraction into a single spatial frequency component. We define SIM patterns on a small subset of DMD mirrors, the unit cell, which is tiled across the DMD by a pair of lattice vectors, $\mathbf{r}_1$ and $\mathbf{r}_2$, which have integer components. This produces a periodic pattern in the sense that mirrors separated by $n\mathbf{r}_1 + m\mathbf{r}_2$ for any $n, m \in \mathbb{Z}$ will be in the same state.

The lattice structure implies all frequency components of the SIM pattern are multiples of the reciprocal lattice vectors, $\mathbf{k}_{1,2}$ which are defined by the property $\mathbf{r}_i \cdot \mathbf{k}_j = \delta_{ij}$ (37). This further constrains the possible frequencies of the diffracted electric field to the set $\mathbf{f} = n_1\mathbf{k}_1 + n_2\mathbf{k}_2$. Furthermore, the Fourier components can be calculated by considering only the unit cell U, which is typically much smaller than the full DMD,

$$\tilde{P}(s,t) = \sum_{(i,j)\in U} P(i,j)\exp\left[-2\pi i(i,j)\cdot(s\mathbf{k}_1 + t\mathbf{k}_2)\right]. \tag{11}$$

This expression is correct up to a boundary term which is introduced because the unit cell may not perfectly tile the DMD. This term is typically small, unless the unit cell occupies a significant fraction of the DMD surface area.

To choose a SIM pattern, we first ask that the pattern can be perfectly translated to change its phase. This is achieved by requiring $\mathbf{r}_2 = (n,m)n_p$, where n_p is the number of desired SIM phases (18, 19, 22, 23). Next, we construct one unit cell of our pattern by generating a smaller unit cell U_p from the vectors $\mathbf{r}_1$ and $\mathbf{r}_2/n_p$. By construction U_p is contained in U. Setting all pixels in U_p to "on" and all other pixels in U to "off" creates the desired pattern. The Fourier components of this pattern are given by

$$\tilde{P}(s,t) = \sum_{(i,j)\in U_p} \exp\left[-2\pi i(i,j)\cdot(s\mathbf{k}_1 + t\mathbf{k}_2)\right]. \tag{12}$$

The strongest non-zero frequency of this pattern matches the reciprocal lattice vector $\mathbf{k}_2$, implying that this vector defines the SIM frequency and angle. However, the pattern also has finite Fourier weight at a number of other reciprocal lattice vectors. If our pattern were defined in continuous space, these components would vanish for all $s \neq 0$, but the pixelation introduces nonzero values. It is vital to prevent these parasitic Fourier components from one SIM pattern from overlapping with the main order of any other pattern because this will lead to projected patterns which have additional structure in addition to the dominant sinusoidal component. Parasitic orders must be blocked in the experiment by inserting a mask in the Fourier plane.

Equation 12 in combination with the reciprocal lattice vectors and eq. 3 defines the forward model for SIM pattern projection.

To generate appropriate SIM patterns for the experiment we construct $\mathbf{r}_{1,2}$ such that $\mathbf{k}_2$ matches a desired period P and angle θ. A full discussion of the pattern generation algorithm is included in Supplemental Note 3.

2.3. Optical transfer function determination. SIM reconstruction relies on detailed knowledge of the optical transfer function, which is typically only known theoretically or inferred from the point-spread function with low resolution. We utilize our DMD and SIM pattern forward models to directly measure the optical transfer function by projecting a sequence of SIM patterns (including parasitic diffraction orders) on a fluorescent sample and comparing the strength of different Fourier components with our model predictions.

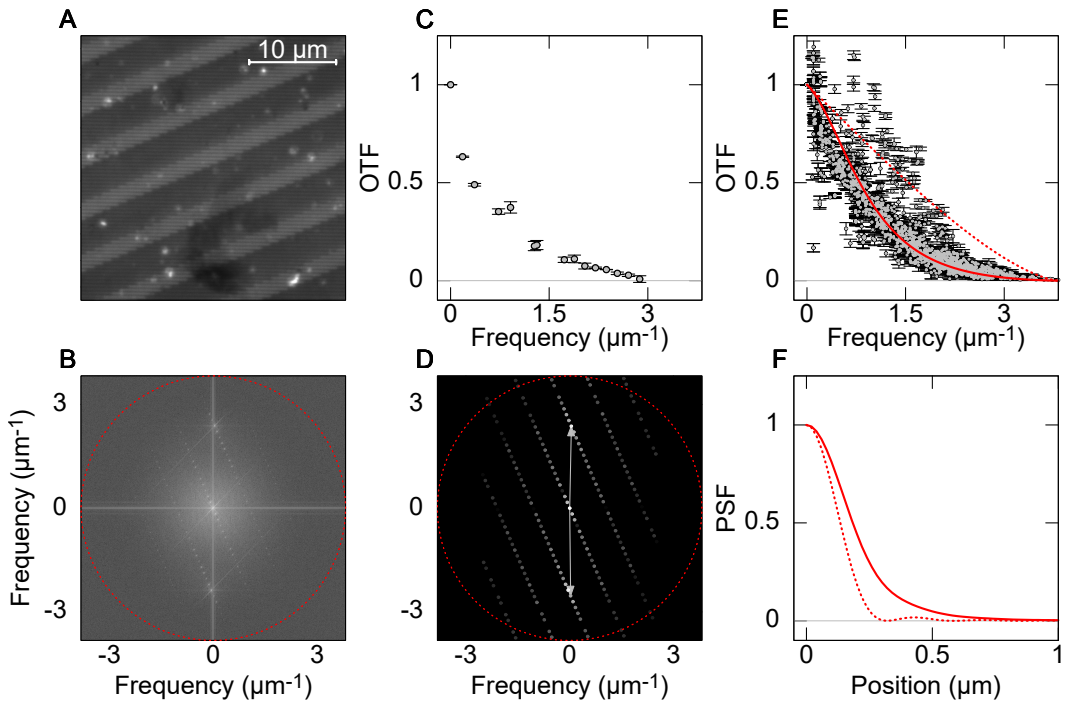

Fig. 2. Experimental optical transfer function determination. **A**. Image of Alexa Fluor 647 dye slide excited with $473\,\mathrm{nm}$ light and a DMD pattern with lattice vectors $\mathbf{r}_1 = (-107, -106)$ and $\mathbf{r}_2 = (111, 117)$. **B**. Power spectrum of image from A. illustrating the discrete set of frequencies the DMD diffracts the pattern into. **C**. Peak heights obtained from the Fourier transform of A. divided by the expected intensity components of the DMD pattern. Only peaks that are expected to be larger than $2.5\,\%$ of the DC value are shown. These provide an experimental estimate of the optical transfer function (gray points). Error bars are estimated from the noise power beyond the band cutoff. **D**. Squares of intensity Fourier components of DMD pattern. These values are used to normalize the measurements from B. to obtain the experimental OTF. Arrows point along the reciprocal lattice vectors $\mathbf{k}_1$ and $\mathbf{k}_2$. The set of discrete frequency components predicted by the forward model matches that seen in the experiment. **E**. Experimental OTF from a set of more than 2000 peaks from 360 images using different patterns (gray circles) and the OTF's as described in C. The solid red line is a parameterized fit to the experimental data shown here. The functional form is described in the text. The dashed red line is the theoretical optical transfer function for a circular aperture and $\mathrm{na} = 1.3$. **F**. Point spread functions corresponding to the OTF's shown in C. and E., including the ideal PSF for a circular aperture (dashed red line) and the PSF corresponding to the parameterized OTF fit (solid red line).

This approach requires careful calibration of the affine transformation between the DMD and the camera coordinates, which we obtain by projecting a test pattern of well-separated spots on the DMD. Each spot is formed by a small "circular" pattern of radius 1.5 mirrors. We perform Gaussian fits to these spots in the camera image. Additional image markers prevent ambiguities due to reflection and inversion. We then determine the affine transformation using Gaussian elimination.

To map the optical transfer function, we project a series of SIM patterns with different frequencies and angles on a sample slide containing a thin layer of Fluorscein, TRITC, or Alexa Fluor 647 dye and observe the response at the camera. To avoid additional complications, we remove all polarization optics along the DMD path. For each pattern, we extract the amplitudes of the Fourier peaks at many reciprocal lattice vectors. We normalize the peak heights by the DC pattern component to correct for laser intensity drift. Finally, we compare the result to the Fourier components of the intensity pattern, as predicted by our forward model. The ratio of the measured and predicted peak value gives the optical transfer function of the imaging system. The results of this measurement for Alexa Fluor 647 are shown in Fig. 2.

The forward model for intensity at the imaging plane is the convolution of the electric field predicted by the DMD forward model band limited by the excitation imaging system optical transfer function. The projected intensity components are given by the autocorrelation of this signal, and the final imaged intensity is additionally blurred by the detection system OTF

$$I(\mathbf{f}) = H_{\mathrm{det}}(\mathbf{f}) \sum_{\mathbf{s}} E(\mathbf{s}) E^*(\mathbf{f}-\mathbf{s})\ \mathrm{circ}\left(\frac{|\mathbf{s}|}{f_{\mathrm{max}}}\right)\ \mathrm{circ}\left(\frac{|\mathbf{f}-\mathbf{s}|}{f_{\mathrm{max}}}\right) \quad \textbf{(13)}$$

$$= H_{\mathrm{det}}(\mathbf{f}) \sum_{\mathbf{s}} \tilde{P}(\mathbf{s}) \tilde{P}^*(\mathbf{f}-\mathbf{s})\ H_{\mathrm{DMD}}(\mathbf{s}) H^*_{\mathrm{DMD}}(\mathbf{f}-\mathbf{s})\, \mathrm{circ}\left(\frac{|\mathbf{s}|}{f_{\mathrm{max}}}\right)\ \mathrm{circ}\left(\frac{|\mathbf{f}-\mathbf{s}|}{f_{\mathrm{max}}}\right), \quad \textbf{(14)}$$

where $\mathbf{f}$ are restricted to the reciprocal lattice vectors of the projected pattern, and the $E(\mathbf{f})$ can be obtained from eq. 12. When working with the $473\,\mathrm{nm}$ or $635\,\mathrm{nm}$ light, the corrections from H_{DMD} are small out to the band limit. We neglect possible aberrations in the illumination point spread function. However, these could be included in systems where they are relevant.

We empirically model the measured optical-transfer function as a Lorentzian times the ideal optical transfer function generated by the Airy point-spread function,

$$h(\mathbf{f}) \quad = \quad \frac{1}{1+\gamma^2|\mathbf{f}|^2} \times h_o(\mathbf{f}). \tag{15}$$

The Lorentzian attenuates the optical-transfer function at high frequencies. This functional form is convenient because it ensures that the OTF is unity at $\mathbf{f} = 0$, zero at $|\mathbf{f}| = f_{\mathrm{max}}$ and monotonically decreasing. The parameter γ, which controls the width of the Lorentzian, is determined by a non-linear least-squares fit.

This functional form assumes the OTF is azimuthally symmetric which is appropriate here because we find no evidence for a strong angular dependence in the experimental data. Nevertheless, a non-parametric OTF may be determined by smoothing and interpolating the data shown in Fig. 2F for systems which do not possess azimuthal symmetry.

3: Experimental results

We designed a DMD SIM microscope for three-color coherent light operation based on the theoretical approach described above. We realize three-color imaging at $473\,\mathrm{nm}$, $532\,\mathrm{nm}$, and $635\,\mathrm{nm}$ over a $125\,\mu\mathrm{m} \times 125\,\mu\mathrm{m}$ field of view using a $100\times$ objective with $\mathrm{na} = 1.3$. Details of the optical path are given in Supplemental Note 1. We have validated our approach by performing SIM on a variety of samples, including test samples to assess our resolution and fixed cells (Supplemental Notes 2, 7) to demonstrate SR enhancement in biological systems.

To support our instrument, we created a Python-based software for forward models of DMD diffraction and pattern projection, DMD pattern design, OTF measurement analysis, simulation of SIM imaging given a ground truth structure, and 2D SIM reconstruction. We benchmarked our approach using a variety of simulations (Supplemental Note 6) as well as compared to FairSIM (Supplemental Note 5). Our approach is built on previously published works, with enhancements based on our ability to precisely calibrate fringe projection and direct measurement of the OTF at each wavelength. All analysis code is available on GitHub `https://github.com/QI2lab`.

3.1. Estimating SIM resolution from variably spaced line pairs. We assessed the experimental SIM resolution by measuring the Argo-SIM test slide (Fig. 3). This slide includes test patterns consisting of variably spaced lines, ranging from $390\,\mathrm{nm}$ to $0\,\mathrm{nm}$ in steps of $30\,\mathrm{nm}$. There are four of these patterns in different orientations (0°, 45°, 90°, 135°), allowing determination of the SIM resolution in all directions (Fig. 3A). We only assess performance in the $473\,\mathrm{nm}$ channel because the other channels do not efficiently excite fluorescence in the sample.

The smallest line pair we resolve is separated by $120\,\mathrm{nm}$ (10th pair, Fig. 3E). This should be compared with the minimum line spacing resolved by the widefield image, which is the $270\,\mathrm{nm}$ spaced pair (5th). The upper theoretical bound on SIM resolution is set by the pattern spacing. The maximum theoretical resolution for $\lambda \sim 520\,\mathrm{nm}$ and $\mathrm{na} = 1.3$ is $\sim 100\,\mathrm{nm}$. Our choice of SIM pattern period $250\,\mathrm{nm}$–$260\,\mathrm{nm}$ further reduces the maximum expected resolution to $\sim 110\,\mathrm{nm}$. We do not saturate this bound due to the maximum signal-to-noise ratio we achieve in the experiment, which is limited by available laser power and the fluorescence of the sample. Experimental resolution in SIM is strongly influenced by signal-to-noise ratio, which is determined by the illumination intensity and sample properties. The highest frequency super resolution information falls at the edge of the OTF, and the intensity must exceed the background noise to be detectable. We further explored the role of signal-to-noise ratio and the use of our calibrated OTF via simulations (Supplemental Note 6).

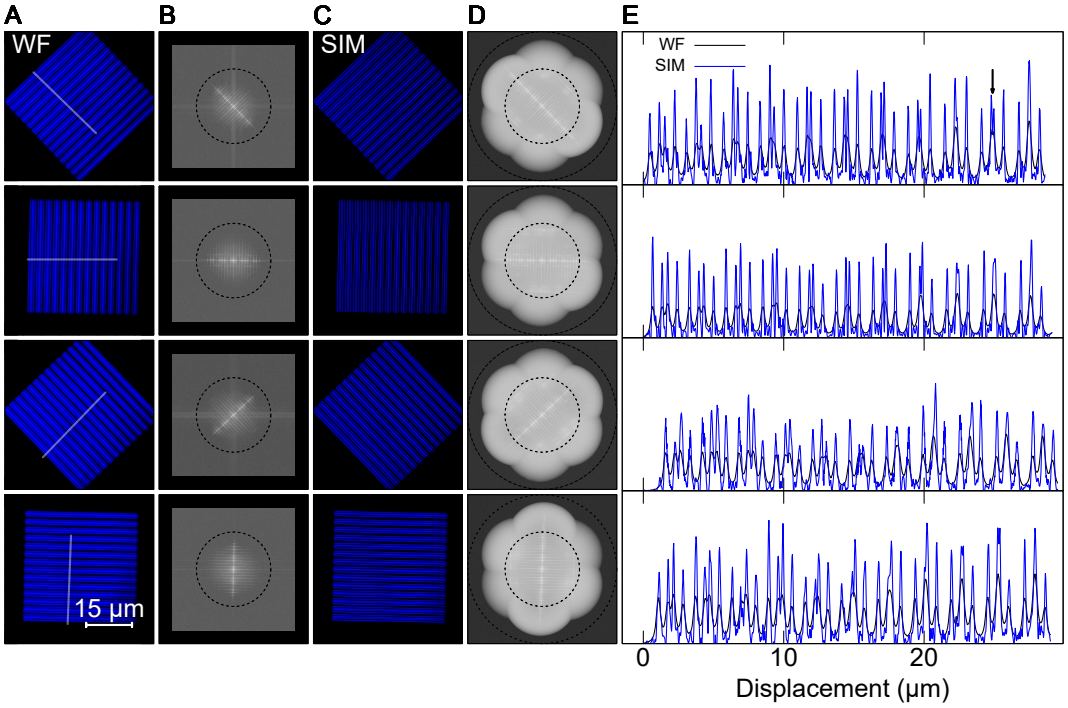

Fig. 3. Experimental characterization of SIM resolution. A. Widefield images for $473\,\mathrm{nm}$ excitation light and different pattern orientations shown in analog-to-digital units (ADU). **B**. Power spectra of the images from A. The black circle illustrates the maximum frequency where the ideal optical transfer function has support for $\mathrm{na} = 1.3$ and emission wavelength $519\,\mathrm{nm}$. For comparison with the SIM power spectrum, the widefield power spectrum is shown on the same frequency axes. Due to the sampling rate, the widefield image does not contain the highest frequencies present in the SIM image. We display a black background for these higher frequencies. **C**. SR-SIM images. **D**. Power spectra of SR-SIM images from D. The smaller circle as in B. The larger circle has twice the diameter, representing the maximum theoretical resolution for (linear) SIM. **E**. One-dimensional cuts plotted along the lines illustrated in A., showing 11 line pairs with spacings ranging from $390\,\mathrm{nm}$ to $90\,\mathrm{nm}$ in $30\,\mathrm{nm}$ steps. We show the widefield image (black) and SR-SIM image (blue). The 5th line pair, with spacing $270\,\mathrm{nm}$, is the closest spaced pair visible in the widefield. The arrow in the top panel identifies 10th line pair, with spacing $120\,\mathrm{nm}$, which is the closest spaced line pair we distinguish in the SR-SIM reconstructions.

3.2. Two-wavelength imaging of fixed cells. As an initial test of multicolor imaging using both "on" and "off" states of the DMD, we performed two wavelength SIM using the $473\,\mathrm{nm}$ and $532\,\mathrm{nm}$ channels to image actin filaments and mitochondria labelled with Alexa Fluor 488 and MitoTracker Red CMXRos in fixed bovine pulmonary artery endothelial (BPAE) cells. The SIM images substantially narrow the apparent width of the actin filaments (Fig. 4), in many cases making two filaments visible that were not distinguishable in the widefield image. The mitochondria similarly reveal cristae which cannot be distinguished in the widefield, but are clearly visible in the SIM. Some high frequency noise is visible in the line cuts (Fig. 4C). The strength of this contribution is set by the Wiener filter parameter, which is chosen empirically to provide a compromise between reducing noise without obscuring low-signal SR information. We verified our reconstruction results using FairSIM (Supplemental Figure 2) and further explored signal-to-noise in filamentous networks via simulation (Supplemental Note 6).

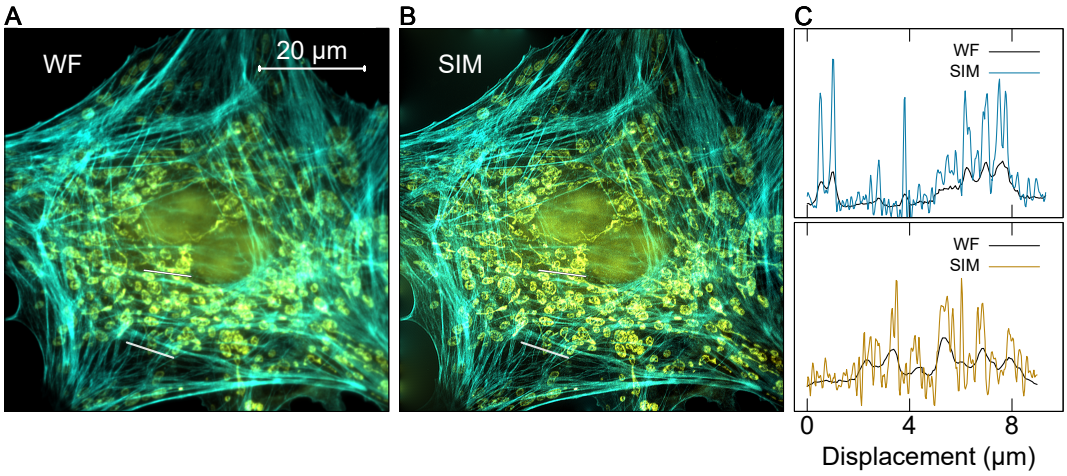

Fig. 4. Two-color imaging of BPAE cells A. Widefield image of a BPAE cell showing actin filaments in the $473\,\mathrm{nm}$ channel (cyan), and mitochondria in the $532\,\mathrm{nm}$ channel (yellow). Images are displayed in ADU. **B**. SIM-SR reconstruction corresponding to the image in A. **C**. One-dimensional cuts plotted along the lines illustrated in A. and B. We show the widefield image (black line) and SR-SIM image (colored line) for the $473\,\mathrm{nm}$ excitation (top) corresponding to the lower line in A. and $532\,\mathrm{nm}$ excitation (bottom) corresponding to the upper line in A. The SIM traces show significant enhancement of resolution and features which cannot be distinguished in the widefield image.

3.3. Three-wavelength imaging of fixed cells. We realized three-wavelength SIM using the $473\,\mathrm{nm}$, $532\,\mathrm{nm}$, and $635\,\mathrm{nm}$ channels to image β-actin, HIF, and FGF18 labelled with Alexa Fluor 488, Alexa Fluor 555, and Alexa Fluor 647 in fixed primary rat endothelial cells. We have previously studied angiogenic signaling in primary rat, sheep, and human endothelial cells using high-throughput multi-wavelength widefield microscopy (38–40).

The SIM results (Fig. 5) show resolution enhancement in all three channels, with the most significant enhancement in the details of the HIF distribution from the $532\,\mathrm{nm}$ channel. Weaker labeling in this sample, as compared with the BPAE cells, results in less resolution enhancement than in that case, particular for the β-actin in the $473\,\mathrm{nm}$ channel.

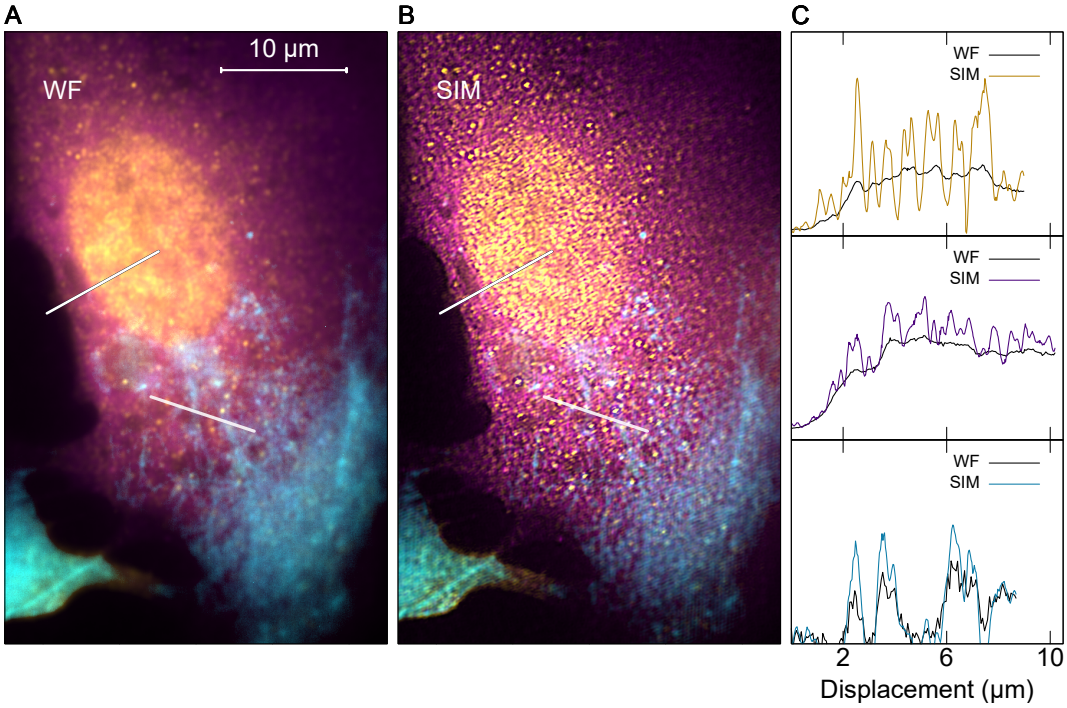

Fig. 5. Three-color imaging of fixed primary rat endothelial cells. A. Composite widefield image with the $473\,\mathrm{nm}$ channel (cyan), $532\,\mathrm{nm}$ channel (yellow), and $635\,\mathrm{nm}$ channel (magenta). Images are shown in ADU. White lines illustrate the position of the line cut shown in C. **B**. SR-SIM images. **C**. One-dimensional cuts plotted along the lines illustrated in A. for $532\,\mathrm{nm}$ (top), $635\,\mathrm{nm}$ (middle), and $473\,\mathrm{nm}$ excitations. $473\,\mathrm{nm}$ and $532\,\mathrm{nm}$ channel line cuts correspond to the upper line cut in A., and $635\,\mathrm{nm}$ to the lower cut.

4: Discussion

Multi-wavelength coherent SIM is regularly achieved using diffraction gratings or SLM's for fringe projection. The maximum achievable pattern display rate is limited by the physical translation and rotation of the grating or the refresh rate of the SLM. Here, we provide a new theoretical framework to use a DMD as the diffractive optic for multi-wavelength coherent SIM, extending previous work (25, 26). This opens the possibility for quantitative, multi-wavelength pattern formation at rates up to $20\,\mathrm{kHz}$ for a factor of ~ 5 lower cost than SLM based units. While SIM imaging rates are ultimately limited by signal-to-noise ratio and phototoxicity, fast control of multi-wavelength pattern formation also provides new avenues in the design of multi-wavelength tomography (41, 42), multi-wavelength optical trapping (43–45), high-speed tracking of photostable fluorescent labels below the diffraction limit (46), and high-speed modulation enhanced localization microscopy in mutiple colors (5, 29, 47). Our work significantly differs from previous SIM approaches using multi-wavelength incoherent LED light sources or multi-wavelength incoherent image projection using a DMD (27, 28). In the current work, the maximum resolution is governed by the coherent transfer function and does not require hundreds to thousands of raw images to generate a SIM image, or require scanning.

Paired with our forward model for DMD diffraction, we developed new calibration tools for diffractive optics used as amplitude only modulators. Exploiting the discrete nature of the DMD mirrors, we created a pattern suite and computational routine to directly map the microscope OTF. Through simulations and experimental verification, we showed that using the known OTF provides a more accurate reconstruction within the actual limits of the optics (Supplemental Note 6).

We demonstrated three-color DMD SIM with coherent light by imaging calibration samples and fixed cell samples. Measurements of the Argo-SIM calibration sample show our instrument produces SR information in all spatial directions and achieves resolution near the theoretical limit. Measurements of fixed cells demonstrate two- and three-color imaging with substantial SIM resolution enhancement. We further verify our results by comparing our algorithm and FairSIM on fixed cell samples. Simulations demonstrate that when the full theoretical SIM resolution is not achieved, this is typically due to low SNR obscuring the necessary SR information (Supplemental Note 6 and Figures 3 and 4). Achieving sufficient SNR is the primary challenge to video-rate multicolor DMD SIM.

Future improvements to our approach may include high power lasers to offset light losses in the optical train, extension to more wavelengths and 3D-SIM (22, 23), online GPU processing to speed reconstruction (21), specialized pattern generation to account for rolling shutters (48), and multiple cameras to speed multi-wavelength acquisition. Ease of alignment and instrument flexibility could be improved by removing the need for the Fourier mask. This could be achieved by developing a SIM reconstruction algorithm capable of accounting for the parasitic diffraction peaks, an approach that would require a detailed DMD forward model such as the one presented here.

5: Conclusion

In this work, we developed a forward model of multicolor DMD diffraction. Using this analytical approach, we proposed and validated a forward model for SIM using a DMD. These advancements allowed us to rigorously determine the allowed optical configurations for multicolor operation and develop a framework to directly measure the microscope OTF. Using simulations, we showed that the use of the real instrument OTF during SIM reconstruction provides a tangible benefit at low signal-to-noise ratios. We performed 2D linear SIM on a variety of samples, including the first demonstration of multicolor coherent 2D SIM imaging with a DMD, using a homebuilt, hardware-triggered microscope. This work broadens potential applications of DMD SIM and opens new possibilities to create highly flexible multi-modal microscopes based around a DMD diffractive element.

Acknowledgments

We thank Drs. Randy Bartels, Thomas Huser, Marcel Müller, and Andrew York for helpful discussions on the use of a DMD as an active diffractive element.

Funding Information

National Heart Lung Blood Institute (NIH NHLBI) (R01HL068702).
Arizona State University (ASU) (Startup funding).

Author contributions

Theoretical model, numerical simulations, hardware design and construction, software development, and instrument validation: PTB. Sample preparation and imaging: RK, GJS, PTB, DPS. Original concept, project management, and writing of manuscript: PTB, DPS.

Disclosures

The authors declare no conflicts of interest.

References

1. George Patterson, Michael Davidson, Suliana Manley, and Jennifer Lippincott-Schwartz. Superresolution imaging using single-molecule localization. *Annual Review of Physical Chemistry*, 61:345–367, 2010. ISSN 0066-426X, 1545-1593. doi: 10.1146/annurev.physchem.012809.103444.
2. Jonatan Alvelid and Ilaria Testa. Fluorescence microscopy at the molecular scale. *Current Opinion in Biomedical Engineering*, 12:34–42, December 2019. ISSN 2468-4511. doi: 10.1016/j.cobme.2019.09.009.
3. T Dertinger, R Colyer, G Iyer, S Weiss, and J Enderlein. Fast, background-free, 3D super-resolution optical fluctuation imaging (SOFI). *Proceedings of the National Academy of Sciences of the United States of America*, 106(52):22287–22292, December 2009. ISSN 0027-8424, 1091-6490. doi: 10.1073/pnas.0907866106.
4. Siân Culley, Kalina L Tosheva, Pedro Matos Pereira, and Ricardo Henriques. SRRF: Universal live-cell super-resolution microscopy. *The International Journal of Biochemistry & Cell Biology*, 101:74–79, August 2018. ISSN 1357-2725, 1878-5875. doi: 10.1016/j.biocel.2018.05.014.
5. Loïc Reymond, Thomas Huser, Verena Ruprecht, and Stefan Wieser. Modulation-enhanced localization microscopy (meLM). *Journal of Physics: Photonics*, June 2020. ISSN 2515-7647. doi: 10.1088/2515-7647/ab9eac.
6. Rainer Heintzmann and Christoph G. Cremer. Laterally modulated excitation microscopy: improvement of resolution by using a diffraction grating. In Irving J. Bigio, Herbert Schneckenburger, Jan Slavik, Katarina Svanberg, and Pierre M. Viallet, editors, *Optical Biopsies and Microscopic Techniques III*. SPIE, jan 1999. doi: 10.1117/12.336833.
7. M. G. L. Gustafsson. Surpassing the lateral resolution limit by a factor of two using structured illumination microscopy. *Journal of Microscopy*, 198(2):82–87, may 2000. doi: 10.1046/j.1365-2818.2000.00710.x.
8. Brent Bailey, Daniel L. Farkas, D. Lansing Taylor, and Frederick Lanni. Enhancement of axial resolution in fluorescence microscopy by standing-wave excitation. *Nature*, 366(6450):44–48, nov 1993. doi: 10.1038/366044a0.
9. M. A. A. Neil, R. Juškaitis, and T. Wilson. Method of obtaining optical sectioning by using structured light in a conventional microscope. *Optics Letters*, 22 (24):1905, dec 1997. doi: 10.1364/ol.22.001905.
10. M.A.A. Neil, R. Juškaitis, and T. Wilson. Real time 3D fluorescence microscopy by two beam interference illumination. *Optics Communications*, 153(1-3): 1–4, jul 1998. doi: 10.1016/s0030-4018(98)00210-7.
11. Mats G. L. Gustafsson, David A. Agard, and John W. Sedat. Doubling the lateral resolution of wide-field fluorescence microscopy using structured illumination. In Jose-Angel Conchello, Carol J. Cogswell, Andrew G. Tescher, and Tony Wilson, editors, *Three-Dimensional and Multidimensional Microscopy: Image Acquisition Processing VII*. SPIE, may 2000. doi: 10.1117/12.384189.
12. J. T. Frohn, H. F. Knapp, and A. Stemmer. True optical resolution beyond the Rayleigh limit achieved by standing wave illumination. *Proceedings of the National Academy of Sciences*, 97(13):7232–7236, jun 2000. doi: 10.1073/pnas.130181797.
13. J. T. Frohn, H. F. Knapp, and A. Stemmer. Three-dimensional resolution enhancement in fluorescence microscopy by harmonic excitation. *Optics Letters*, 26 (11):828, jun 2001. doi: 10.1364/ol.26.000828.
14. Mats G.L. Gustafsson, Lin Shao, Peter M. Carlton, C. J. Rachel Wang, Inna N. Golubovskaya, W. Zacheus Cande, David A. Agard, and John W. Sedat. Three-dimensional resolution doubling in wide-field fluorescence microscopy by structured illumination. *Biophysical Journal*, 94(12):4957–4970, jun 2008. doi: 10.1529/biophysj.107.120345.
15. L. Schermelleh, P. M. Carlton, S. Haase, L. Shao, L. Winoto, P. Kner, B. Burke, M. C. Cardoso, D. A. Agard, M. G. L. Gustafsson, H. Leonhardt, and J. W. Sedat. Subdiffraction multicolor imaging of the nuclear periphery with 3D structured illumination microscopy. *Science*, 320(5881):1332–1336, jun 2008. doi: 10.1126/science.1156947.
16. Peter Kner, Bryant B Chhun, Eric R Griffis, Lukman Winoto, and Mats G L Gustafsson. Super-resolution video microscopy of live cells by structured illumination. *Nature Methods*, 6(5):339–342, apr 2009. doi: 10.1038/nmeth.1324.
17. Liisa M. Hirvonen, Kai Wicker, Ondrej Mandula, and Rainer Heintzmann. Structured illumination microscopy of a living cell. *European Biophysics Journal*, 38 (6):807–812, jun 2009. doi: 10.1007/s00249-009-0501-6.
18. Ronny Förster, Hui-Wen Lu-Walther, Aurélie Jost, Martin Kielhorn, Kai Wicker, and Rainer Heintzmann. Simple structured illumination microscope setup with high acquisition speed by using a spatial light modulator. *Optics Express*, 22(17):20663, aug 2014. doi: 10.1364/oe.22.020663.
19. Hui-Wen Lu-Walther, Martin Kielhorn, Ronny Förster, Aurélie Jost, Kai Wicker, and Rainer Heintzmann. fastSIM: a practical implementation of fast structured illumination microscopy. *Methods and Applications in Fluorescence*, 3(1):014001, jan 2015. doi: 10.1088/2050-6120/3/1/014001.
20. Michael Shaw, Lydia Zajiczek, and Kevin O'Holleran. High speed structured illumination microscopy in optically thick samples. *Methods*, 88:11–19, oct 2015. doi: 10.1016/j.ymeth.2015.03.020.
21. Andreas Markwirth, Mario Lachetta, Viola Mönkemöller, Rainer Heintzmann, Wolfgang Hübner, Thomas Huser, and Marcel Müller. Video-rate multi-color structured illumination microscopy with simultaneous real-time reconstruction. *Nature Communications*, 10(1), sep 2019. doi: 10.1038/s41467-019-12165-x.
22. Lin Shao, Peter Kner, E Hesper Rego, and Mats G L Gustafsson. Super-resolution 3D microscopy of live whole cells using structured illumination. *Nature Methods*, 8(12):1044–1046, oct 2011. doi: 10.1038/nmeth.1734.
23. R. Fiolka, L. Shao, E. H. Rego, M. W. Davidson, and M. G. L. Gustafsson. Time-lapse two-color 3D imaging of live cells with doubled resolution using structured illumination. *Proceedings of the National Academy of Sciences*, 109(14):5311–5315, mar 2012. doi: 10.1073/pnas.1119262109.
24. Laurence J. Young, Florian Ströhl, and Clemens F. Kaminski. A guide to structured illumination TIRF microscopy at high speed with multiple colors. *Journal of Visualized Experiments*, (111), may 2016. doi: 10.3791/53988.
25. Alice Sandmeyer, Mario Lachetta, Hauke Sandmeyer, Wolfgang Hübner, Thomas Huser, and Marcel Müller. DMD-based super-resolution structured illumination microscopy visualizes live cell dynamics at high speed and low cost. BioRxiv 10.1101/797670, 2019.
26. Ziwei Li, Qinrong Zhang, Shih-Wei Chou, Zachary Newman, Raphaël Turcotte, Ryan Natan, Qionghai Dai, Ehud Y. Isacoff, and Na Ji. Fast widefield imaging of neuronal structure and function with optical sectioning in vivo. *Science Advances*, 6(19):eaaz3870, may 2020. doi: 10.1126/sciadv.aaz3870.
27. Andrew G York, Sapun H Parekh, Damian Dalle Nogare, Robert S Fischer, Kelsey Temprine, Marina Mione, Ajay B Chitnis, Christian A Combs, and Hari Shroff. Resolution doubling in live, multicellular organisms via multifocal structured illumination microscopy. *Nature Methods*, 9(7):749–754, may 2012. doi: 10.1038/nmeth.2025.
28. Dan Dan, Ming Lei, Baoli Yao, Wen Wang, Martin Winterhalder, Andreas Zumbusch, Yujiao Qi, Liang Xia, Shaohui Yan, Yanlong Yang, Peng Gao, Tong Ye, and Wei Zhao. DMD-based LED-illumination super-resolution and optical sectioning microscopy. *Scientific Reports*, 3(1), jan 2013. doi: 10.1038/srep01116.
29. Loïc Reymond, Johannes Ziegler, Christian Knapp, Fung-Chen Wang, Thomas Huser, Verena Ruprecht, and Stefan Wieser. SIMPLE: Structured illumination based point localization estimator with enhanced precision. *Optics Express*, 27(17):24578, aug 2019. doi: 10.1364/oe.27.024578.
30. Seungwoo Shin, Kyoohyun Kim, Jonghee Yoon, and YongKeun Park. Active illumination using a digital micromirror device for quantitative phase imaging. *Optics Letters*, 40(22):5407, nov 2015. doi: 10.1364/ol.40.005407.
31. Michael Chen, David Ren, Hsiou-Yuan Liu, Shwetadwip Chowdhury, and Laura Waller. Multi-layer born multiple-scattering model for 3D phase microscopy. *Optica*, 7(5):394, apr 2020. doi: 10.1364/optica.383030.
32. Humberto González, Lluís Martínez-León, Fernando Soldevila, Ma Araiza-Esquivel, Jesús Lancis, and Enrique Tajahuerce. High sampling rate single-pixel digital holography system employing a dmd and phase-encoded patterns. *Optics express*, 26(16):20342–20350, August 2018. ISSN 1094-4087. doi: 10.1364/OE.26.020342.

33. Philip Zupancic, Philipp M. Preiss, Ruichao Ma, Alexander Lukin, M. Eric Tai, Matthew Rispoli, Rajibul Islam, and Markus Greiner. Ultra-precise holographic beam shaping for microscopic quantum control. *Optics Express*, 24(13):13881, jun 2016. doi: 10.1364/oe.24.013881.
34. Peter T. Brown, Debayan Mitra, Elmer Guardado-Sanchez, Reza Nourafkan, Alexis Reymbaut, Charles-David Hébert, Simon Bergeron, A.-M. S. Tremblay, Jure Kokalj, David A. Huse, Peter Schauß, and Waseem S. Bakr. Bad metallic transport in a cold atom Fermi-Hubbard system. *Science*, 363(6425):379–382, dec 2018. doi: 10.1126/science.aat4134.
35. Texas Instruments. Using lasers with DLP DMD technology. *TI DN*, 2509927, 2008.
36. R. Casini and P. G. Nelson. On the intensity distribution function of blazed reflective diffraction gratings. *Journal of the Optical Society of America A*, 31(10): 2179, sep 2014. doi: 10.1364/josaa.31.002179.
37. Neil W. Ashcroft and N. David Mermin. *Solid State Physics*, chapter 5. The Reciprocal Lattice, pages 85–94. Cengage Learning, Inc, 1976.
38. Megan A Ahern, Claudine P Black, Gregory J Seedorf, Christopher D Baker, and Douglas P Shepherd. Hyperoxia impairs pro-angiogenic RNA production in preterm endothelial colony-forming cells. *AIMS Biophysics*, 4(2):284–297, 2017. ISSN 2377-9098. doi: 10.3934/biophy.2017.2.284.
39. Christina Kim, Gregory J Seedorf, Steven H Abman, and Douglas P Shepherd. Heterogeneous response of endothelial cells to insulin-like growth factor 1 treatment is explained by spatially clustered sub-populations. *Biology Open*, 8(11), November 2019. ISSN 2046-6390. doi: 10.1242/bio.045906.
40. Gregory Seedorf, Christina Kim, Bradley Wallace, Erica W Mandell, Taylor Nowlin, Douglas Shepherd, and Steven H Abman. rhIGF-1/BP3 preserves lung growth and prevents pulmonary hypertension in experimental bronchopulmonary dysplasia. *American Journal of Respiratory and Critical Care Medicine*, 201 (9):1120–1134, May 2020. ISSN 1073-449X, 1535-4970. doi: 10.1164/rccm.201910-1975OC.
41. Shwetadwip Chowdhury, Will J Eldridge, Adam Wax, and Joseph A Izatt. Structured illumination microscopy for dual-modality 3D sub-diffraction resolution fluorescence and refractive-index reconstruction. *Biomedical Optics Express*, 8(12):5776–5793, December 2017. ISSN 2156-7085. doi: 10.1364/BOE.8.005776.
42. Seungwoo Shin, Doyeon Kim, Kyoohyun Kim, and Yongkeun Park. Super-resolution three-dimensional fluorescence and optical diffraction tomography of live cells using structured illumination generated by a digital micromirror device. *Scientific Reports*, 8(1):9183, June 2018. ISSN 2045-2322. doi: 10.1038/s41598-018-27399-w.
43. Furqan M Fazal and Steven M Block. Optical tweezers study life under tension. *Nature Photonics*, 5:318–321, May 2011. ISSN 1749-4885. doi: 10.1038/nphoton.2011.100.
44. Matthew J Comstock, Taekjip Ha, and Yann R Chemla. Ultrahigh-resolution optical trap with single-fluorophore sensitivity. *Nature Methods*, 8(4):335–340, April 2011. ISSN 1548-7091, 1548-7105. doi: 10.1038/nmeth.1574.
45. Cecilia Muldoon, Lukas Brandt, Jian Dong, Dustin Stuart, Edouard Brainis, Matthew Himsworth, and Axel Kuhn. Control and manipulation of cold atoms in optical tweezers. *New Journal of Physics*, 14(7):073051, jul 2012. doi: 10.1088/1367-2630/14/7/073051.
46. Knut Drescher, Jörn Dunkel, Luis H Cisneros, Sujoy Ganguly, and Raymond E Goldstein. Fluid dynamics and noise in bacterial cell-cell and cell-surface scattering. *Proceedings of the National Academy of Sciences of the United States of America*, 108(27):10940–10945, July 2011. ISSN 0027-8424, 1091-6490. doi: 10.1073/pnas.1019079108.
47. Jelmer Cnossen, Taylor Hinsdale, Rasmus Ø Thorsen, Marijn Siemons, Florian Schueder, Ralf Jungmann, Carlas S Smith, Bernd Rieger, and Sjoerd Stallinga. Localization microscopy at doubled precision with patterned illumination. *Nature methods*, 17(1):59–63, January 2020. ISSN 1548-7091, 1548-7105. doi: 10.1038/s41592-019-0657-7.
48. Liyan Song, Hui-Wen Lu-Walther, Ronny Förster, Aurélie Jost, Martin Kielhorn, Jianying Zhou, and Rainer Heintzmann. Fast structured illumination microscopy using rolling shutter cameras. *Measurement Science and Technology*, 27(5):055401, apr 2016. doi: 10.1088/0957-0233/27/5/055401.